43rd AIAA Aerospace Sciences Meeting and Exhibit, Jan 10–Jan 13, Reno, Nevada

Analysis of Shockwave/Turbulent Boundary Layer Interaction Using DNS and Experimental Data

M. Wu*, P. Bookey†, M.P. Martin‡ and A.J. Smits§

Princeton University, Princeton, NJ 08540

Shockwave/turbulent boundary layer interactions are studied by comparing direct numerical simulation and experimental data. Two canonical configurations, a 24-degree compression ramp and shock impinging a wall with reflection, are studied. The Mach number for the incoming boundary layer is 2.9. Re_θ in the numerical simulation is 2400. Two experimental data sets are used, namely those of Bookey et al[1] at the same flow conditions as the DNS and those of Selig[2] at Re_θ of about 70,000. Mean velocity profiles, wall pressure distribution, mass flux turbulence intensity, 2D density correlation and locations of the flow separation and reattachment are compared. In addition, an analysis of the turbulence structure characteristics for the DNS data is given.

I. Introduction

The study of shockwave/turbulent boundary layer interaction (STBLI) is of great importance in engineering applications, for example, in scramjet engines, where the turbulent flow inside the engine is characterized by complex shock patterns. Many aspects of STBLI such as shock unsteadiness, turbulence amplification and mean flow modification induced by shock distortion, separation and reattachment criteria, are not fully understood. Accurate predictions and scaling laws, and effective means to control the interaction regions can only be achieved by understanding the fundamental physics governing the dynamics of shockwave/turbulent boundary layer interactions.

Many experimental efforts have been performed on STBLI during the 70's and 80's. For example, Settles et al[3–6] and Dolling & Bogdonoff[7] did experiments on compression ramp and swept fin configurations to study 2D and 3D STBLI problems. Also Smits and Muck[8] did experiments on compression ramps of different turning angles to investigate turbulence amplification. Recently, with the rapid development of computer speed and capacity, direct numerical simulation (DNS) of STBLI has become affordable and can be used to study fundamental physical phenomena. Adams[9] performed the DNS of a compression ramp flow at Re_θ=1685. However, most of the experimental data available were at much higher Reynolds numbers, making it difficult to draw definite conclusions from direct comparison of the experimental and computational data. To address these issues, we are performing a joint numerical and experimental study of STBLI, where the simulation and experimental conditions, including Reynolds numbers and Mach numbers, are matched. We are also comparing our DNS data with higher Reynolds number experimental data to investigate possible Reynolds number effects in the STBLI problems.

*Graduate Student, Student Member AIAA.

†Graduate Student, Student Member AIAA.

‡Assistant Professor, Member AIAA.

§Professor, Member AIAA.

Table 1. Domain size and grid points for the DNS data, where x, y and z correspond to streamwise, spanwise and wall-normal directions.

Case	L_x/δ	L_y/δ	L_z/δ	N_x	N_y	N_z
Ramp	13	2	4.5	412	128	96
Reflect 1	15.8	2	4.5	412	128	128
Reflect 2	15	2	7.4	412	128	96

In this paper, we present the analysis of two STBLI configurations: a 24-degree compression ramp and a shock impinging a wall with reflection. The data include that of DNS[10,11] and experiments[1] at the same flow conditions. In addition, experimental data at higher Reynolds numbers are also considered.[2,3,12,13] The paper is organized as follows. The canonical configurations are detailed in Section II. The numerical method, initialization procedure and boundary conditions are given in Section III. The statistics resulting from the DNS data are compiled in Section IV. The comparison of the DNS data with experiments are given in Sections V and VI at the same and higher Reynolds number conditions, respectively. An analysis of the turbulent structure characteristics using DNS data is given in Section VII. A summary and conclusions are given in Section VIII.

II. Flow Configurations

Two canonical configurations have been chosen to study STBLI: (1) a compression ramp and (2) a reflected shock with separation and turbulent slip layer. Figure 1 shows sketches of the two configurations. The turning angle for the compression ramp is 24 degrees. The angle of the wedge that is used to generate the oblique shock in the reflected shock configuration is 12 degrees.

Numerical errors associated with the discrete evaluation of the Jacobian matrices might be amplified through the simulation. Therefore we use analytical transformations to generate the grids and to minimize these errors. For the compression ramp case, the transformations are chosen to make the grid clustered near the wall in the wall-normal direction and near the ramp corner in the streamwise direction. For the reflected shock case, the grid is made to be clustered near both the lower and upper walls. In the streamwise direction, the grid is nearly equally spaced. Figure 2 shows sample grids for the compression ramp and reflected shock cases. These transformations are discussed in detail in Martin et al[14] and Wu & Martin.[11]

Figures 3a and 3b show the computational domains for the compression ramp and reflected shock cases, respectively. The length in the wall-normal direction is about 4.5δ for both cases, where δ is the thickness of the incoming boundary layer. In the spanwise direction, the domain size is 2δ. For the ramp case, the corner is 7δ away from the inlet. The length along the ramp is 6δ. As for the reflected shock case, the wedge used to generated the oblique shock is placed at 5δ downstream from the inlet. The total length in the streamwise direction is about 15.8δ. The dashed parallelograms indicate the locations of the rescaling stations, which are at 4δ downstream of the inlet in both cases.

For the reflected shock case, the domain size is constrained by the numerical setup. Thus, consider an additional configuration as shown in Figure 4. The computational domain size is 15δ in streamwise direction, 7.4δ in the wall-normal direction and 2δ in the spanwise direction. The rescaling station is also located at a distance 4δ away from the inlet. The grid is uniform in streamwise and spanwise directions. In the wall-normal direction the grid is geometrically stretched. For this configuration, the impinging shock is not generated by a wedge. Rather, it is imposed on the inflow profile. The removal of the top wall allows for a smaller number of grid points and a longer domain downstream of the interaction. The computational

Table 2. Incoming boundary layer parameters.

Case	δ (mm)	δ^* (mm)	θ (mm)	C_f
Ramp	0.85	0.255	0.063	2.04×10^{-3}
Reflect	0.85	0.275	0.064	1.95×10^{-3}

domain size and number of grid points are summarized in Table 1.

III. Numerical Method and Boundary Conditions

A 3rd-order, bandwidth-optimized WENO (Weighted Essential Non-oscillatory) scheme[15] is used to approximate the convective flux terms in the governing equations. This scheme has been designed for high bandwidth and low dissipation, while being a shock capturing scheme. These properties are necessary for the DNS of turbulent flows at the Mach numbers that we consider. A 4th-order standard central scheme is used to compute the viscous terms. As for the time integration, we use a 2nd-order DP-LUR (Data Parallel Lower-Upper Relaxation) method.[16] The combined numerical algorithm has been shown to give accurate results for the DNS of compressible turbulence.[17–19]

Initial conditions

Prescribing and controlling the initial flow conditions computationally has received a great deal of attention. The initialization procedure is sketched in Figure 5. The first step is to get an initial flow field for the incoming boundary layer. A RANS calculation is performed to get the mean flow quantities. Then the fluctuations are obtained by transforming the turbulence of a Mach 0.3 turbulent boundary layer DNS data to that of the desired Mach number using Morkovin's scaling laws and the strong Reynolds analogy (SRA). We run the incoming boundary layer during a DNS until it reaches a stationary state. After that, we interpolate the flow field of the incoming boundary layer onto the inlet of the grids for the STBLI cases. Then, the last profile of the inlet is copied to the rest of the computational domain to get the initial flow field for the STBLI cases. The initialization procedure for the STBLI is also discussed in the paper of Martin et al[14] and Wu & Martin.[11] Details about the initial transformations for the incoming boundary layer data can be found in Martin's 2003 and 2004 papers.[17,19]

Boundary conditions

To get a continuous incoming turbulent flow and maintain the upstream inflow conditions, a rescaling method for compressible flows was developed by Xu and Martin.[20] The main idea of the rescaling method is to take a profile at some place downstream of the computational domain and rescale it using scaling laws, then put it back to the inlet to get continuous inflow data. At the outlet, we use the sponge layer technique[21] together with supersonic exit conditions to minimize flow reflections. The sponge layer is about 1δ in length at the outlet. Inside the sponge layer region, a term is added to the RHS of the governing equations.

$$\vec{Z} = -\sigma(x)(\vec{U} - \vec{U}_0) \tag{1}$$

where

$$\sigma(x) = A_s(N_s+1)(N_s+2)\frac{(x-x_s)^{N_s}(L_x-x)}{(L_x-x_s)^{N_s+2}} \tag{2}$$

Typically A_s=3 and N_s=4. At the top boundary, we also use supersonic exit boundary conditions. In the spanwise direction, periodic boundary conditions are used. The wall boundaries are isothermal.

IV. DNS Statistics

The DNS statistics have been presented in Wu and Martin[10,11] and are briefly summarized here. The flow conditions for the incoming boundary layers are freestream Mach number of 2.9, Re_θ=2400, $\rho_e = 0.71$ kg/m^3, T_e= 251 K, and $T_w = 633.4$. The resulting parameters for the boundary layers at the inlet of both simulations are given in Table 2. The errors in C_f are less than 5% comparing with the Van-Driest skin friction coefficient formula. Figure 6 shows the Van-Driest transformed mean velocity profile for the incoming boundary layer. We can see good agreement with the log law, indicating that the boundary layer is well resolved. Figure 7 plots a sequence of $|\nabla\rho|$ contour for the compression ramp case to illustrate the shock unsteady motion. Time increases from (a) to (f). The interval between each frame is about $2\delta/U_\infty$. Similar to Figure 7, Figures 8 and 9 show the shock motion in the reflected shock case for the old and new configurations, respectively. Figure 10 shows Van-Driest transformed velocity profiles at different streamwise locations for both cases. Open and closed symbols indicate the locations upstream and downstream of the interactions, respectively. There is a characteristic 'dip' in the log region for the mean velocity profile downstream of the interaction. This is an indication that after the interaction the Karman constant increases with distance from the wall. This is consistent with the experimental observations of Smits and Muck[8] at $Ma = 2.9$ and $Re_\delta = 1,640,000$. Figure 11 plots the mass flux turbulence intensity upstream and downstream of the interactions for both cases. Downstream of the interactions, the maximal values of the mass flux turbulence intensity are amplified by a factor of about 5 and 3 for the compression ramp and reflected shock case, respectively.

V. Comparison with experiments under the same flow conditions

Experiments for the compression ramp and reflected shock case have been performed by Bookey et al[1] in Princeton Gasdynamics Laboratory using the Low Turbulence Variable Geometry(LTVG) wind tunnel, which has the capability of achieving low Reynolds number flow conditions. The experiments have the same flow configurations and conditions as the DNS cases, ie. freestream Mach 2.9, Re_θ about 2400 and isothermal wall boundaries.

Figure 12 shows filtered Rayleigh scattering images from the experiments and density contour plots from DNS data for both STBLI cases. We observe similar structures in the incoming boundary layers and near the interaction regions. Figure 13 shows the comparison of Van-Driest transformed velocity profiles in the incoming boundary layers. The agreement is very good except in the near wall region where the velocity measurement in the experiment is not accurate. The two-dimensional density correlations are computed to investigate the structures in the incoming boundary layer. Figure 14 shows both correlations from the experiment and DNS for the compression ramp case. The correlations have the same shape and angle, indicating that the structures inside the incoming boundary layer in the experiment and DNS are similar.

VI. Comparison with higher Reynolds number experimental data

It is found that most phenomena in the low Reynolds number experiments are similar to those at high Reynolds number conditions.[1] Here we perform a comparison of the DNS data with the high Reynolds number experimental data.[2,3,12,13] The experimental conditions are freestream Mach number is 2.9 and Re_θ about is 70,000.

Figure 15 shows the comparison of the mass flux turbulence intensity upstream and downstream of the interaction for the compression ramp case. The relative errors are about 20 percent which is a good agreement because the discrepancy factor is within the experimental error. The peeks of the mass flux turbulence intensity in the experiment and DNS are in good agreement. The mass flux turbulence intensity is greatly amplified through the interaction. The amplification factor is about 5 and 4 for Selig's experiment[2] and DNS data , respectively. Figure 16 shows the comparison of skin friction coefficient for the compression ramp case. The DNS and experimental data have different C_f values upstream and downstream of the

interaction because they do not have the same Reynolds number. However, the positions of the separation and reattachment points are in good agreement. This means that the size and location of the separation zone may be Reynolds number independent. Figure 17 shows the wall pressure distribution. The DNS data agree well with the experimental data downstream of the interaction. However, there is a noticeable difference between numerical and experimental data inside the separation region, upstream of the corner. In all the experimental data sets, there is a plateau in the wall pressure distribution shortly after the wall pressure rises. In contrast, this feature is not found in the DNS data. This could be due to the Reynolds number effects. The DNS data of Adams[9] at Re_θ=1685 also show no plateau. This issue is discussed in more detail in the next section.

VII. Turbulence and Shock Structure Characteristics from DNS Data

Figure 18 shows numerical schlieren images for the compression ramp and reflected shock cases, where a numerical schlieren is a density gradient contour plot with nonlinear gray scale mapping to simulate schlieren pictures in experiments. We can see both the shock structure and the structures inside the incoming boundary layer. For the compression ramp case, the schlieren shows that the shock foot penetrates into the boundary layer. For the reflected shock case, there is a complex shock system. Due to viscous effects, the impinging shock is reflected at a point near the boundary layer edge. For both cases, the flapping character of the shock downstream of the interaction can be observed from the slope of the downstream shock. For the additional configuration of the reflected shock case, the grid is geometrically stretched in the wall-normal direction. Therefore the grid spacing is large near the top edge of the computational domain. Thus, the impinging and reflected shocks are diffused. They appear thicker than those in the original configuration.

Figure 19 plots an iso-surface of the magnitude of the gradient of pressure for the compression ramp case. It shows the three-dimensional structure of the shock. Notice the that shock curves in both streamwise and spanwise directions showing the three-dimensionality of the shock. Figure 20 plots contours of u' for the compression ramp case at $z^+ = 5$, showing the near-wall streaky structures. Upstream of the interaction the streaks are elongated. Downstream of the interaction, we observe two large structures with a length scale of about δ in the spanwise direction coming out from the interaction region (indicated by dark regions in the plot). To ensure that this result is not an artifact of the spanwise domain size, we doubled the size of the computational domain in the spanwise direction. Again, we observed the same length scale. Thus, the possibility of these structures being caused by the limitation of the spanwise domain size is excluded. Figure 21 is an iso-surface of the magnitude of the gradient of pressure for the reflected shock case. As expected, the impinging shock is quite straight and steady. In contrast, the reflected shock shows small wrinkles. The downstream shock is not so curved as in the compression ramp case. Figure 22 plots contours of u' for the reflected shock case. No three-dimensional structure is observed downstream of the interaction. It is known that concave streamline patterns lead to produce Görtler vortices. We believe that the presence of three-dimensional structures is due to the concave curvature of the streamlines in the compression ramp case, while in the reflected shock case streamlines remain straight. The appearance of near-wall three-dimensional structures in the compression ramp case may be the cause of the spanwise wrinkles in the shock structure shortly downstream of the interaction, as shown in Figure 19.

Figure 23 plots the time-averaged Mach number and density gradient contours for the compression ramp case. As the shock penetrates into the boundary layer, it is diffused and weakened. In the near wall interaction region, the Mach number changes gradually. Figure 24 shows the sonic line (dashed line) and streamlines near the corner for the compression ramp case. Near the corner, the sonic line is about 0.5δ away from the wall. The streamlines show a concave pattern. Therefore the flow is compressed gradually. A possible explanation for the discrepancy of the wall pressure distribution between the low and high Reynolds number data might be as follows. The sonic line inside the incoming boundary layer is found closer to the wall with increasing Reynolds number. Therefore, the strength of the shock at the shock foot will be higher with increasing Reynolds number. In turn, the rise in pressure will be faster and less gradual. The expected shock pattern and pressure jump for high and low Reynolds number data might be sketched as shown in

Figure 25. For high Reynolds number data, there are two strong compressions inside the interaction region. Thus, the wall pressure has two distinct steps, as observed in the experimental data. The first compression is at the onset of the separation. For the low Reynolds number case, however, the flow turns gradually in a concave pattern. Therefore a compression fan instead of a shock is formed and the first distinct compression is not observed. Theory remains to be verified.

VIII. Conclusion

DNS of two STBLI configurations, compression ramp and reflected shock, have been carried out. The results from DNS are compared against experimental data at the same flow conditions. Van-Driest transformed velocity profiles for the incoming boundary layer show good agreement. The two-dimensional correlation for the incoming boundary layer shows similar structure shape and angle. Comparison between the DNS results and higher Re experimental data is also made for the compression ramp case. Mass flux turbulence intensity shows good agreement. Separation and reattachment points agree very well, indicating that the size of the separation bubble may be Reynolds number independent. The turbulence structure shortly downstream of the interaction region exhibits a three-dimensional character for the compression ramp case. This is explained by the streamline curvature for this case. No three dimensionality of the structure is observed for the reflected shock case. Wall pressure distributions show good agreement except that, no plateau is observed inside the separation bubble for the DNS results. This might be due to the Reynolds number effect. In the DNS where Reynolds number is low, the sonic line is farther away from the wall, making the shock weaker inside the boundary layer. While in high Reynolds number cases, two strong shock appear at the separation and reattachment points, making the wall pressure distribution have two rapidly rising regions. Overall, the DNS results agree fairly well with experimental data. Further experimental data at low Reynolds number is still being collected to further analyze the data at low and high Reynolds numbers and to verify our hypothesis.

Acknowledgments

We would like to thank NASA Ames for the use of the DPLR CFD code to generate the turbulent mean flow. This work is supported by the Air Force Office of Scientific Research under grant AF/F49620-02-1-0361.

References

[1]Bookey, P., Wu, M., Smits, A., and Martin, P., "New Experimental Data of STBLI at DNS/LES Accessible Reynolds Numbers," *Extend abstract submitted to the 43rd AIAA Aerospace Sciences Meeting and Exhibit. Reno, N*, January 2005.

[2]Selig, M. S., *Unsteadiness of Shock Wave/Turbulent Boundary Layer Interactions with Dynamic Control*, Ph.D. thesis, Princeton University, 1988.

[3]Settles, G., Vas, I., and Bogdonoff, S., "Details of Shock-Separated Turbulent Boundary Layer at a Compression Corner," *AIAA Journal*, Vol. 14, No. 12, 1976, pp. 1709–1715.

[4]Settles, G., Fitzpartrick, T., and Bogdonoff, S., "Detailed Study of Attached and Separated Compression Corner Flowfields in High Reynolds Number Supersonic Flow," *AIAA Journal*, Vol. 17, No. 6, 1979.

[5]Settles, G., Perkins, J., and Bogdonoff, S., "Investigation of Three-Dimensional Shock/Boundary-Layer Interactions at Swept Compression Corners," *AIAA Journal*, Vol. 18, No. 7, 1980.

[6]Settles, G., Perkins, J., and Bogdonoff, S., "Upstream Influence Scaling of 2D & 3D Shock/Turbulent Boundary Layer Interactions at Compression Corners," *AIAA Paper No. 81-0334*, 1981.

[7]Dolling, D. and Bogdonoff, S., "Upstream Influence Scaling of Sharp Fin-Induced Shock Wave Turbulent Boundary Layer Interactions," *AIAA Paper No. 81-0336*, 1981.

[8]Smits, A. and Muck, K., "Experimental study of three shock wave/turbulent boundary layer interactions," *J. Fluid Mech.*, Vol. 182, 1987, pp. 291–314.

[9]Adams, N., "Direct numerical simulation of turbulent boundary layer along a compression ramp at M=3 and Re_θ=1685," *J. Fluid Mech.*, Vol. 420, 2000, pp. 47–83.

[10]Wu, M. and Martin, P., "Direct Numerical Simulation of Shockwave/Turbulent Boundary Layer Interactions," *AIAA*

Paper No. 2004-2145, 2004.

[11]Wu, M. and Martin, P., "Direct Numerical Simulation of Two Shockwave/Turbulent Boundary Layer Interactions at Mach 2.9 and Re_θ 2400," *submitted to AIAA Journal*, 2004.

[12]Dolling, D. and Murphy, M., "Unsteadiness of the Separation Shock Wave in a Supersonic Compression Ramp Flowfield," *AIAA Journal*, Vol. 21, No. 12, 1983.

[13]Dolling, D. and Or, C., "Unsteadiness of the Shock Wave Structure in Attached and Separated Compression Corner Flow Fields," *AIAA Paper No. 83-1715*, 1983.

[14]Martin, M., Xu, S., and Wu, M., "Preliminary work on DNS and LES of STBLI," *AIAA Paper No. 03-3964*, 2003.

[15]Weirs, G. and Candler, G., "Optimization of Weighted ENO Schemes for DNS of Compressible Turbulence," *AIAA Paper No. 97-1940*, 1997.

[16]Martin, M. P. and Candler, G. V., "A Parallel Implicit Method for the Direct Numerical Simulation of Compressible Flows," *submitted to Journal of Computational Physics*, 2004.

[17]Martin, M., "Preliminary DNS Database of Hypersonic Turbulent Boundary Layers," *AIAA Paper No. 03-3464*, 2003.

[18]Xu, S. and Martin, P., "Assessment of Inflow Boundary Conditions for Compressilbe Boundary Layers," *Physics of Fluids*, Vol. 6, No. 7, 2004.

[19]Martin, M., "DNS of Hypersonic Turbulent Boundary Layers. Part I: Initialization and Comparison with Experiments," *submitted to Journal of Fluid Mechanics, Also AIAA Paper No. 2004-2337*, 2005.

[20]Xu, S. and Martin, M. P., "Inflow Boundary Conditions for Compressible Turbulent Boundary Layers," *AIAA Paper No. 03-3963*, 2003.

[21]Adams, N., "Direct numerical simulation of turbulent compression ramp flow," *Theoretical and Computational Fluid Dynamics*, Vol. 12, 1998, pp. 109–129.

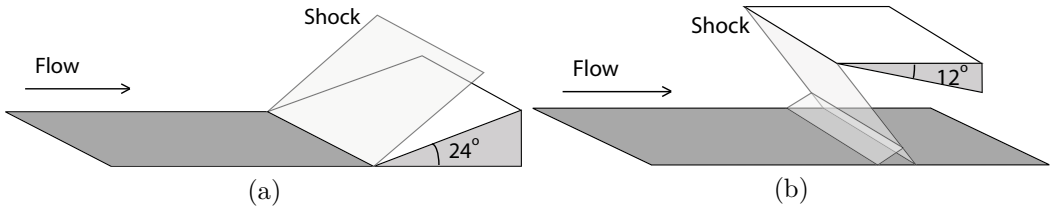

(a) (b)

Figure 1. Configurations for the (a) compression ramp case and (b) reflected shock case.

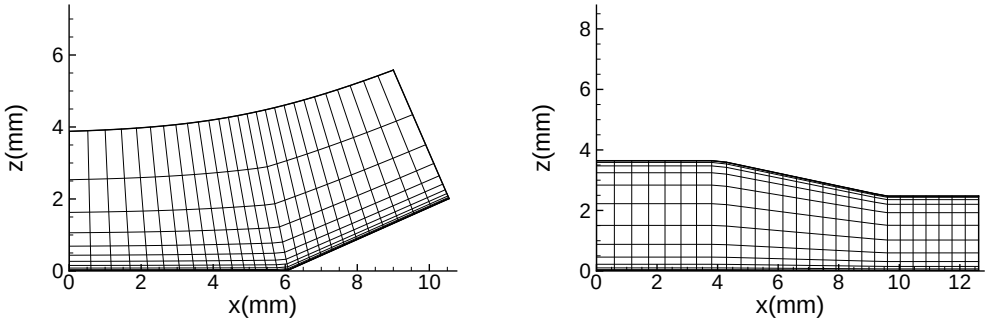

(a) (b)

Figure 2. Computational grids for the (a) compression ramp case and (b) reflected shock case.

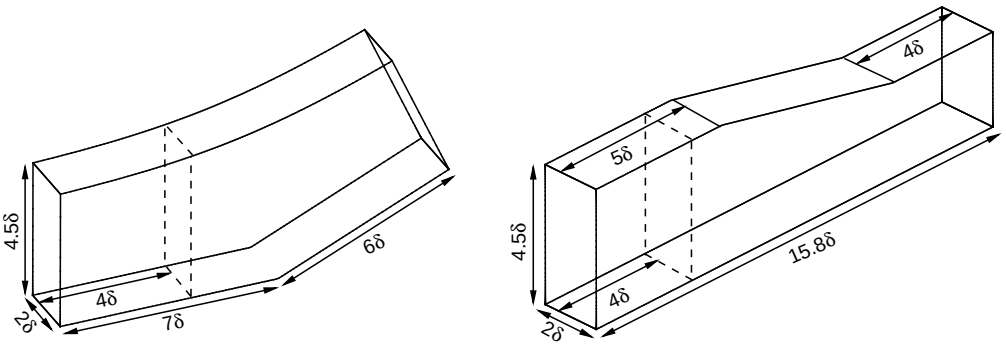

(a) (b)

Figure 3. Computational domains for the (a) compression ramp case and (b) reflected shock case.

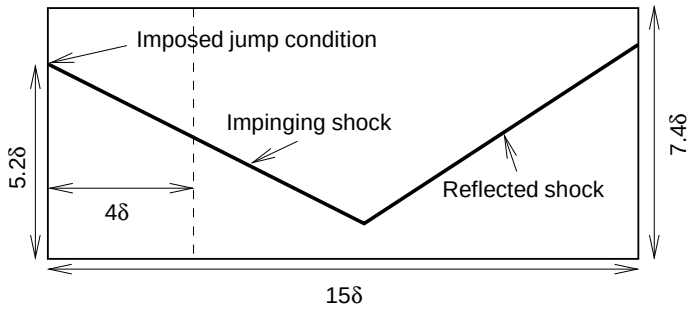

Figure 4. Sketch of the additional numerical setup for the reflected shock case.

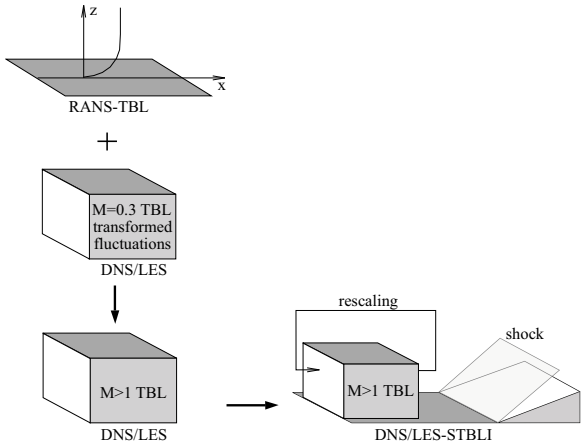

Figure 5. Initialization procedure for STBLI simulations.

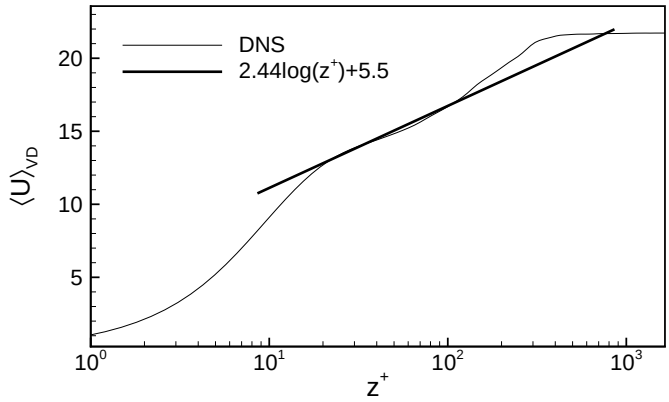

Figure 6. Van-Driest transformed mean velocity profile for the incoming boundary layer.

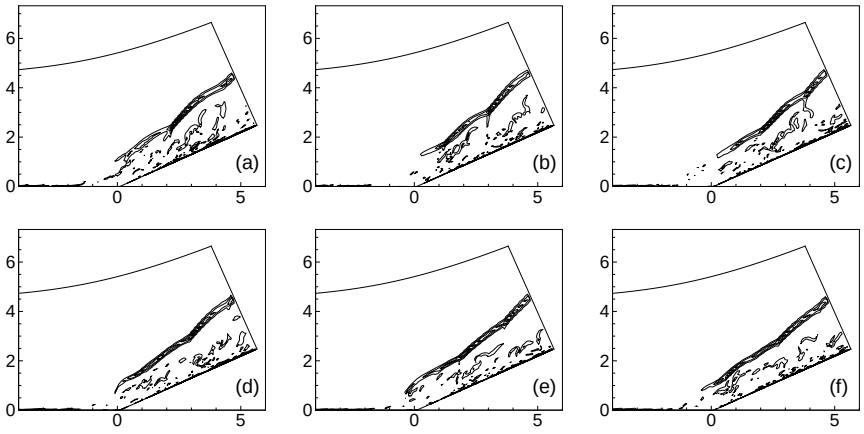

Figure 7. Sequence of $|\nabla\rho|$ contours for the compression ramp case (coordinate unit in δ).

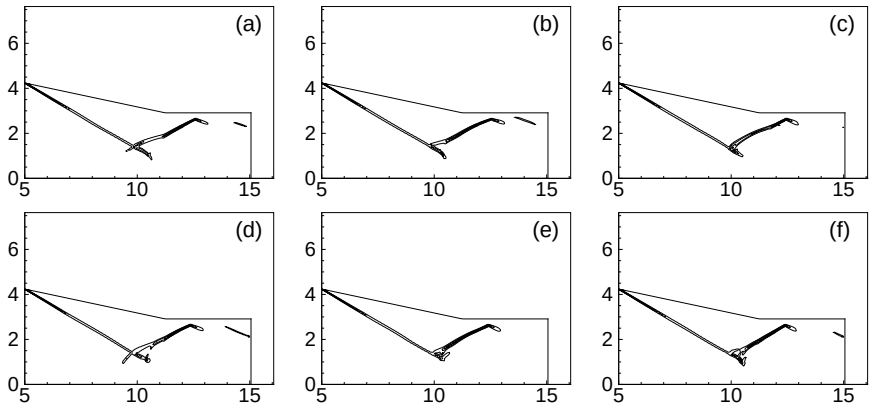

Figure 8. Sequence of $|\nabla\rho|$ contours for the reflected shock case with original setup (coordinate unit in δ).

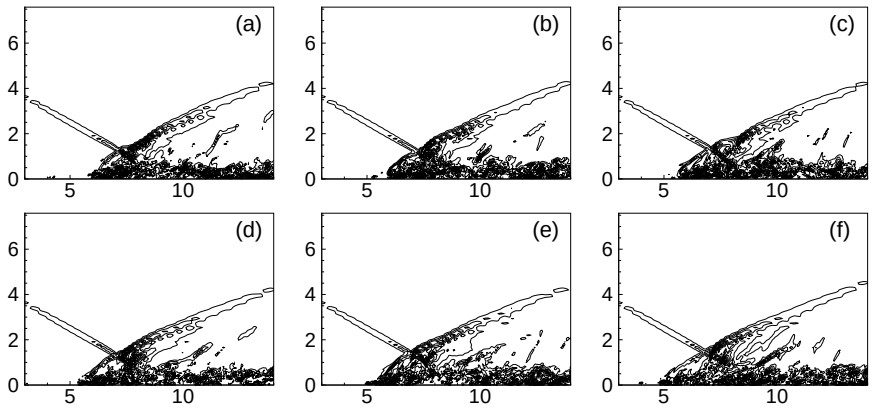

Figure 9. Sequence of $|\nabla\rho|$ contours for the reflected shock case with additional setup(coordinate unit in δ).

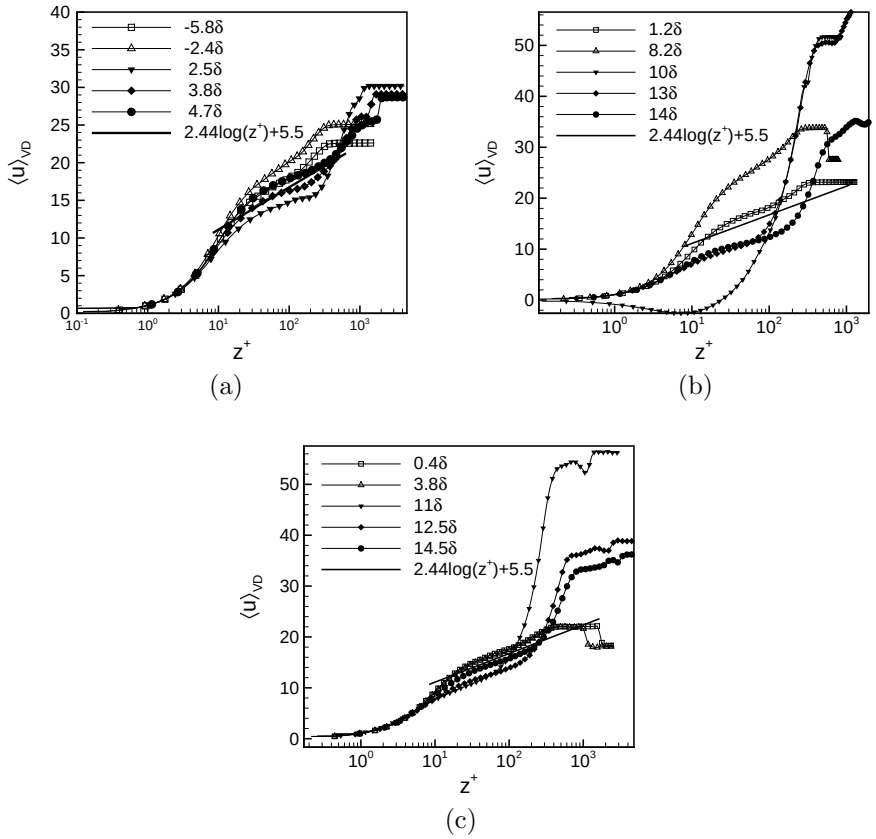

Figure 10. Van-Driest transformed velocity profile at different streamwise locations for the compression ramp (a) , reflected shock with original setup (b) and reflected shock with additional setup (c).

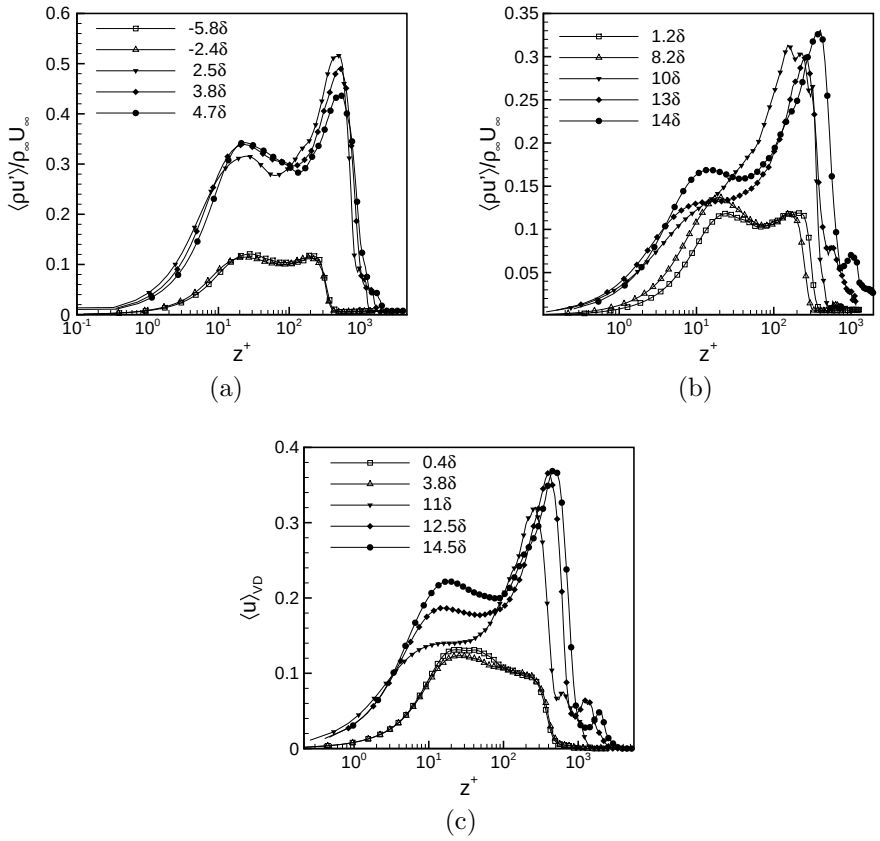

Figure 11. Mass flux turbulence intensity at different streamwise locations for the compression ramp (a) , reflected shock with original setup (b) and reflected shock with additional setup (c).

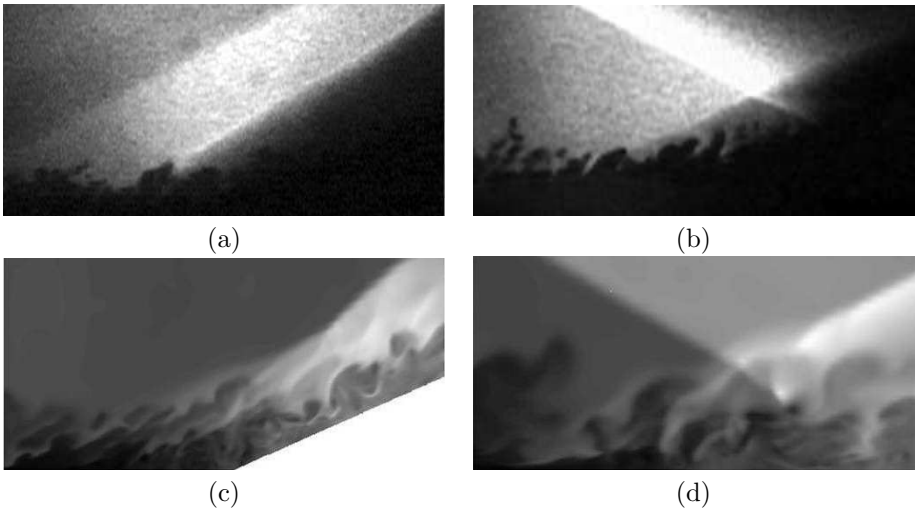

Figure 12. Filtered Rayleigh scattering images for the compression ramp (a) and reflected shock case (b); Density contour plots for the compression ramp (c) and reflected shock case (d).

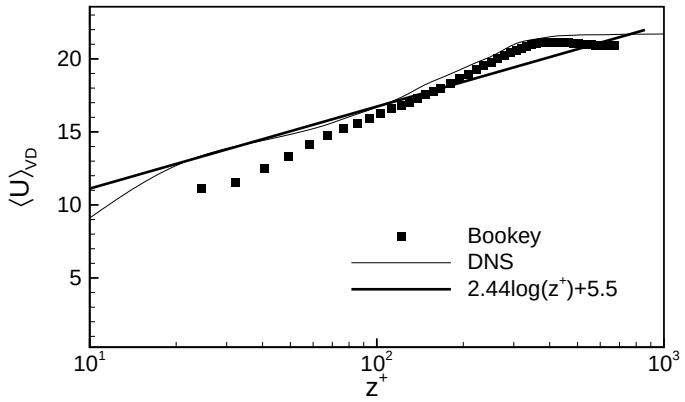

Figure 13. Comparison of the Van-Driest transformed mean velocity profile for the incoming boundary layer.

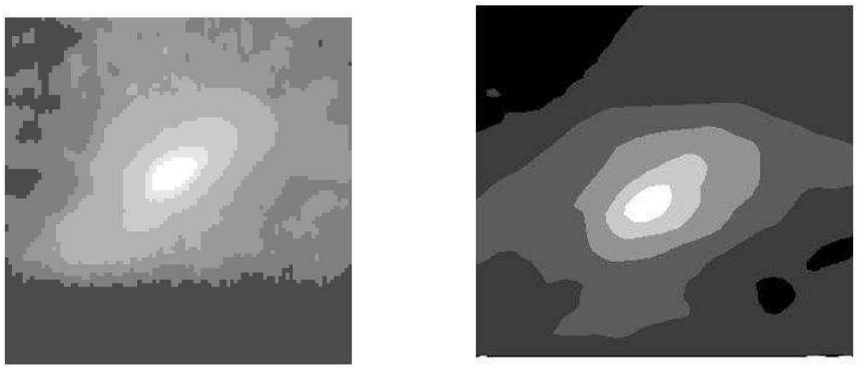

(a) (b)

Figure 14. 2D density correlation from the experiment (a) and DNS data (b).

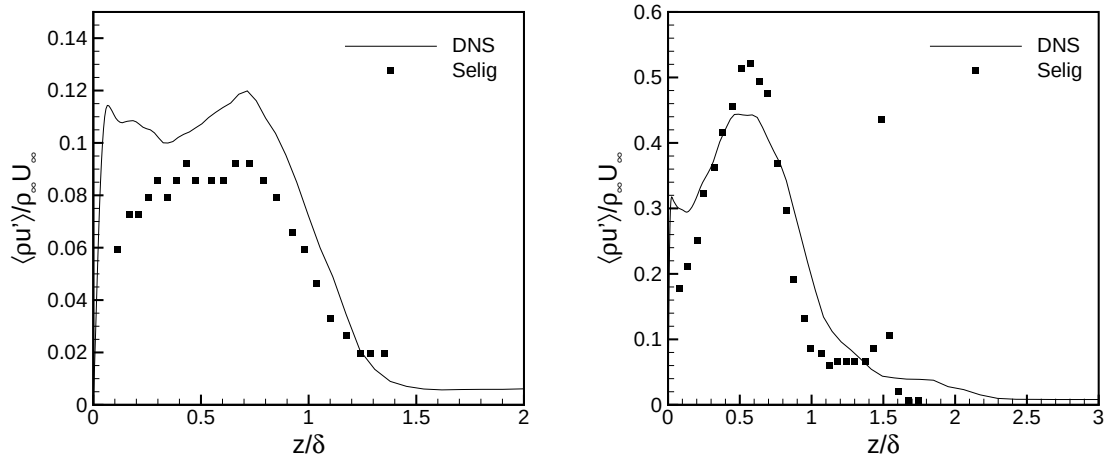

(a) (b)

Figure 15. Comparison of the mass flux turbulence intensity for the compression ramp case upstream (a) and downstream (b) of the interaction. Experimental data from Selig.[2]

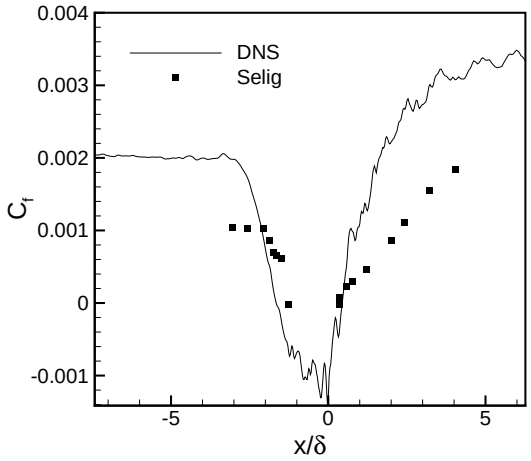

Figure 16. Comparison of the skin friction coefficient for the compression ramp case. Experimental data from Selig.[2]

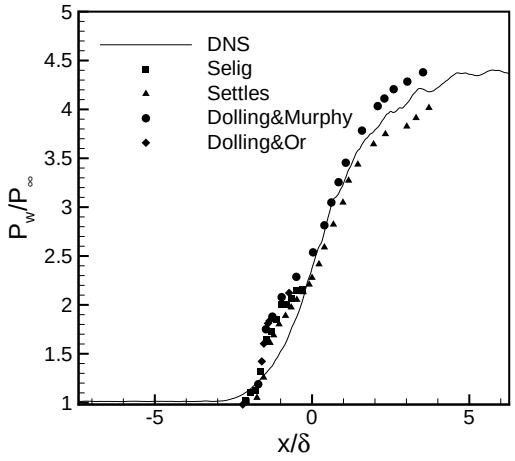

Figure 17. Comparison of the wall pressure distribution for the compression ramp case. Experimental data from Selig,[2] Settles,[3] Dolling & Murphy[12] and Dolling & Or.[13]

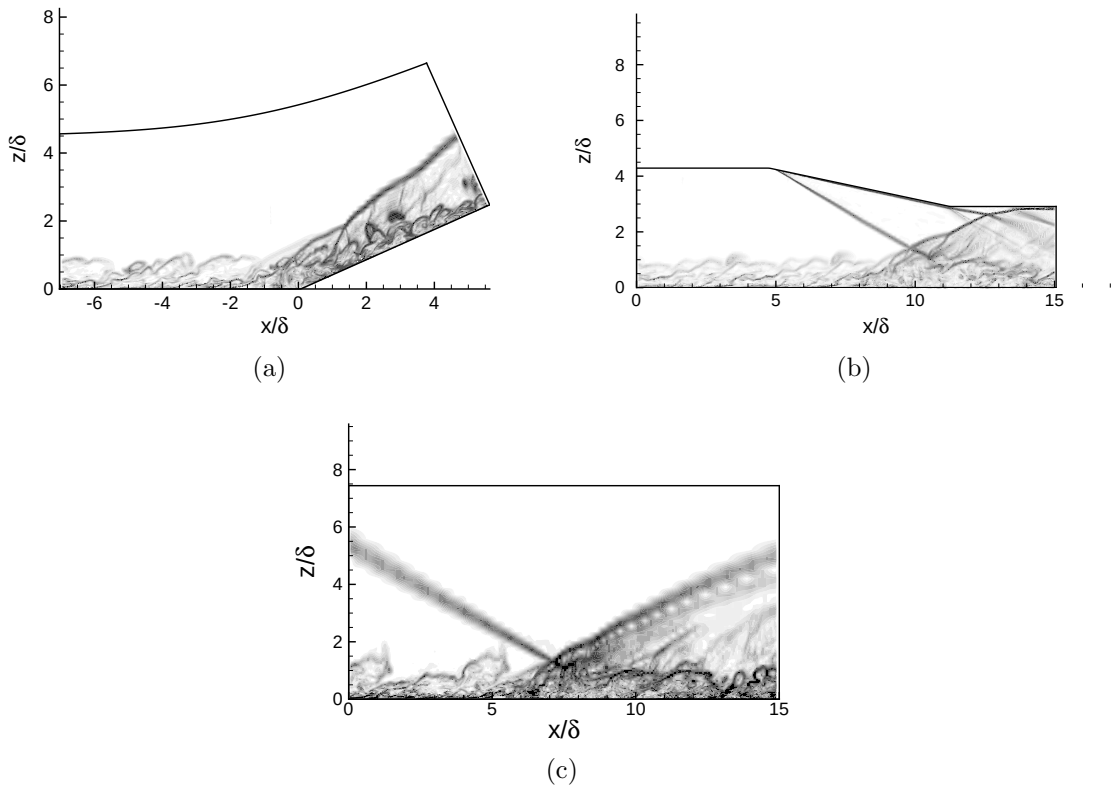

Figure 18. Numerical schlieren images for the compression ramp (a) and reflect shock case with original configuration (b) and additional configuration (c).

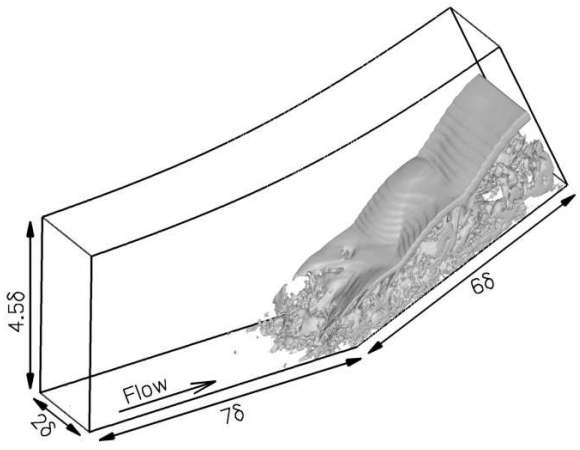

Figure 19. Iso-surface of $|\nabla\rho|$ for the compression ramp case.

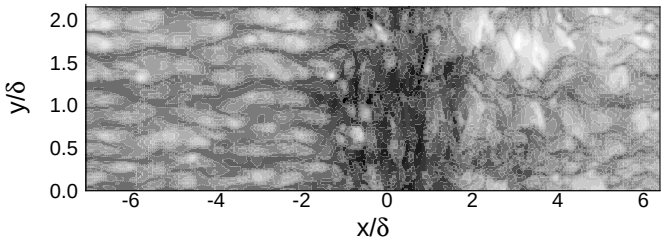

Figure 20. Contour plot of u' for the compression ramp case.

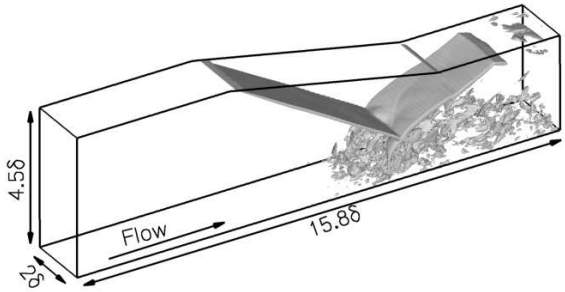

(a)

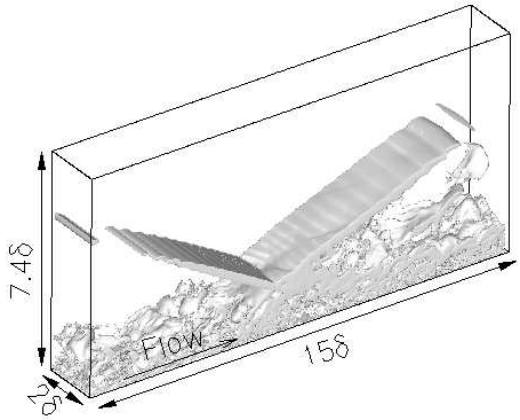

(b)

Figure 21. Iso-surface of $|\nabla\rho|$ for the reflected case: (a) original configuration, (b) additional configuration.

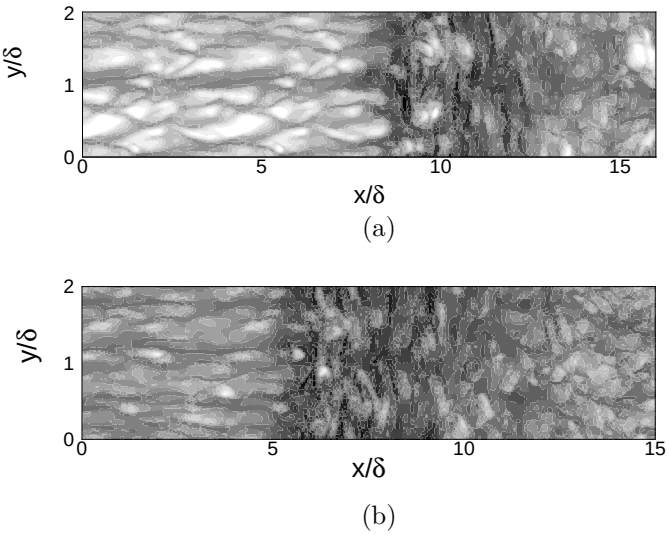

Figure 22. Contour plot of u' for the reflected shock case: (a) original configuration, (b) additional configuration.

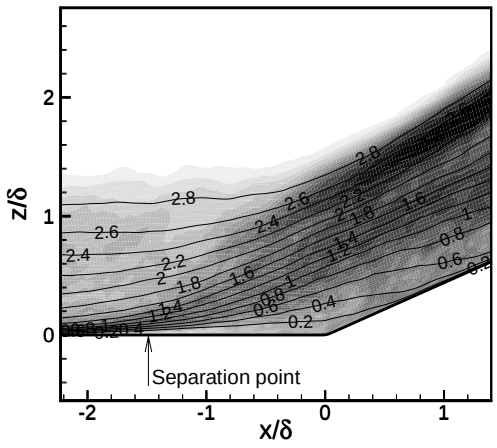

Figure 23. Contour plot of Mach number and density gradient for the compression ramp case.

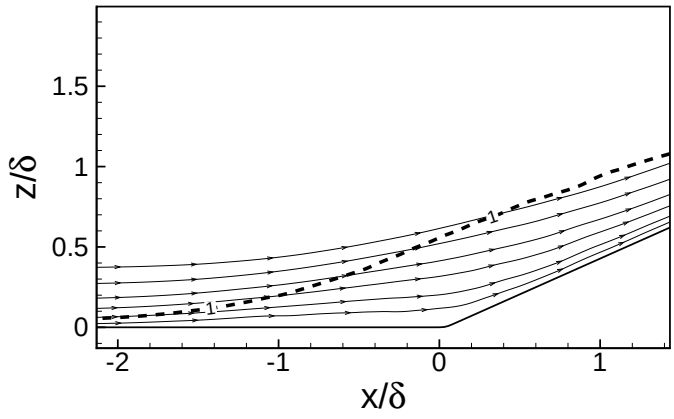

Figure 24. Streamlines and sonic line near the corner for the compression ramp case.

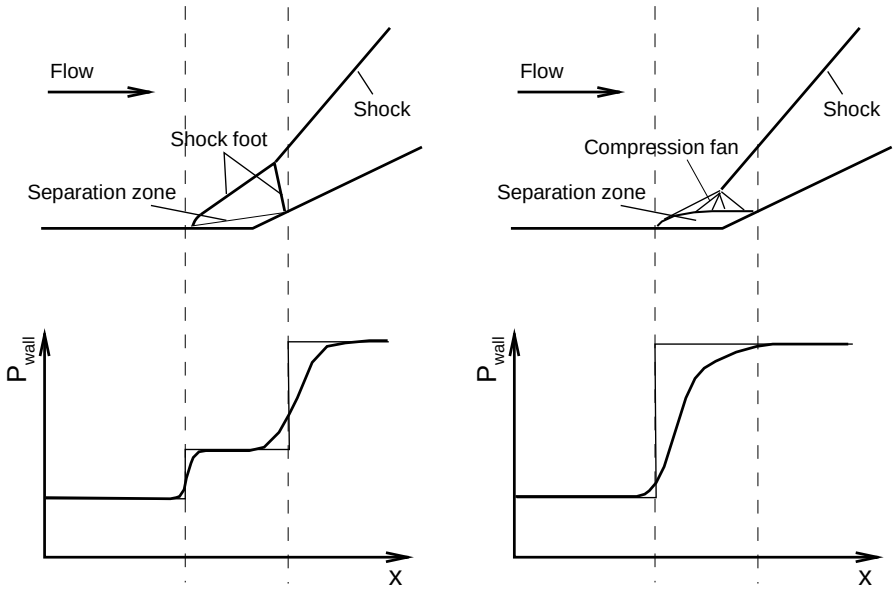

(a) (b)

Figure 25. Sketch of the flow patterns in high (a) and low (b) Reynolds STBLI.